Injectable Biocompatible Zeolite Nanocrystals for Enhanced Tumor Oxygenation and MRI Imaging

Abdallah Amedlous, C Hélaine, Francesco Dalena, Clément Anfray, Thomas Ménard, Isis Blanchard, Jérôme Toutain, Samuel Valable, Svetlana Mintova

▶ **To cite this version:**

Abdallah Amedlous, C Hélaine, Francesco Dalena, Clément Anfray, Thomas Ménard, et al.. Injectable Biocompatible Zeolite Nanocrystals for Enhanced Tumor Oxygenation and MRI Imaging. ACS Applied Materials & Interfaces, 2025, 17 (5), pp.8003-8016. ⟨10.1021/acsami.4c20383⟩. ⟨hal-04920878⟩

HAL Id: hal-04920878

https://normandie-univ.hal.science/hal-04920878v1

Submitted on 30 Jan 2025

HAL is a multi-disciplinary open access archive for the deposit and dissemination of scientific research documents, whether they are published or not. The documents may come from teaching and research institutions in France or abroad, or from public or private research centers.

L'archive ouverte pluridisciplinaire **HAL**, est destinée au dépôt et à la diffusion de documents scientifiques de niveau recherche, publiés ou non, émanant des établissements d'enseignement et de recherche français ou étrangers, des laboratoires publics ou privés.

HAL Authorization

ACS APPLIED MATERIALS & INTERFACES

www.acsami.org

Research Article

Injectable Biocompatible Zeolite Nanocrystals for Enhanced Tumor Oxygenation and MRI Imaging

Abdallah Amedlous,[§] Charly Hélaine,[§] Francesco Dalena, Clément Anfray, Thomas Ménard, Isis Blanchard, Jérôme Toutain, Samuel Valable,* and Svetlana Mintova*

Cite This: https://doi.org/10.1021/acsami.4c20383

Read Online

ACCESS | Metrics & More | Article Recommendations | Supporting Information

ABSTRACT: Tumor hypoxia significantly limits the effectiveness of radiotherapy, as oxygen is crucial for producing cancer-killing reactive oxygen species. To address this, we synthesized nanosized faujasite (PBS-Na-FAU) zeolite crystals using clinical-grade phosphate-buffered saline (PBS) as the solvent, ensuring preserved crystallinity, microporous volume, and colloidal stability. The zeolite nanocrystals showed enhanced safety profiles *in vitro* and *ex vivo*, and *in vivo* studies showed no apparent toxicity to animals. They demonstrated a high oxygen capacity with a release rate of 2.68 mg/L under hypoxic conditions. The introduction of gadolinium (Gd^{3+}) into the zeolite nanocrystals by ion exchange, replacing three monovalent cations (Na^+ and K^+), led to an increased oxygen capacity of the sample. In situ Fourier transform infrared (FTIR) study revealed that Gd-containing zeolite (PBS-Gd-FAU) adsorbed ~23% more oxygen at 20 kPa compared to the as-synthesized sample (PBS-Na-FAU). *In vivo* magnetic resonance imaging (MRI) demonstrated targeted oxygen delivery and release within brain tumors, revealing 14.91 and 17.10% differences in cerebral blood volume (CBV) between tumor and contralateral brain tissue after 15 and 20 min, respectively, compared to the control. *T*1 maps at 7 T indicated a relaxation rate of 9.254 $mM^{-1}{\cdot}s^{-1}$ for PBS-Gd-FAU, twice that of commercial Gd-chelates. These findings highlight the potential of Gd-containing zeolite nanocrystals synthesized in PBS as a biocompatible platform for enhancing tumor oxygenation in anticancer therapy, with significant clinical translation potential.

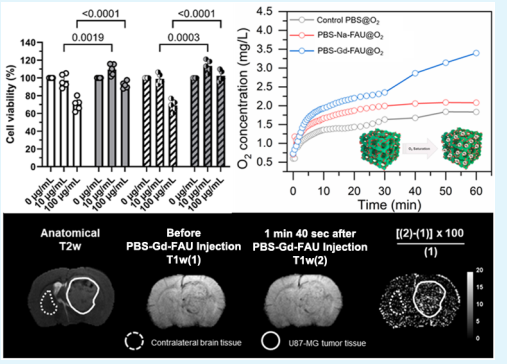

KEYWORDS: *zeolite nanocrystals, saline, synthesis, injectable, biocompatible, oxygen delivery*

Downloaded via INIST-CNRS on January 30, 2025 at 11:04:28 (UTC).
See https://pubs.acs.org/sharingguidelines for options on how to legitimately share published articles.

INTRODUCTION

Nanosized materials have made significant contributions across various biomedical fields, serving as imaging agents, supporting anticancer and antimicrobial therapies, enhancing drug delivery systems, and contributing to tissue engineering.[1−4] These nanomaterials are particularly valuable in medicine due to their small size, which imparts unique physicochemical attributes capable of influencing biological responses.[5,6] For example, the nanoscale dimensions of particles enable phenomena such as the enhanced permeability and retention (EPR) effect, significantly increasing the uptake of drug delivery nanoparticles within tumors[7−9] without targeting the normal tissues. Additionally, nanotextured surfaces have the potential to improve the performance of medical implants, while superparamagnetic nanoparticles can substantially enhance magnetic resonance imaging (MRI) contrast.[1,3] However, as clinical applications of these nanoparticles continue to advance in various medical areas, regulatory agencies demand increasingly biocompatible nanomaterials with the lowest toxicity levels and minimal particle aggregation in biological environments.[7]

Zeolites are crystalline porous materials that have proven to be valuable for many applications, including gas adsorption and separation, sensor technology, and environmental treatment.[10−13] The application of zeolites is designated depending on their physicochemical properties, which consist of chemical composition, pore size, crystalline structure, shape, and size of particles as well as chemical/thermal and colloidal stability. Modulating zeolite size to achieve nanosized particles and employing inorganic cations as structure-directing agents has ushered in a wealth of possibilities for diverse biological applications.[14−17] In recent years, our group, alongside numerous others, has shown significant interest in exploring the preparation and applications of nanosized zeolites in the biomedical field.[17−21] However, as clinical applications of these materials continue to advance across various medical domains, a substantial challenge emerges. Previously, the synthesis of nanozeolites was conducted in water media, which could limit their suitability for clinical use. For instance, even though the previous approach with water-prepared zeolite proved safe for

Received: November 20, 2024
Revised: January 14, 2025
Accepted: January 16, 2025

© XXXX American Chemical Society

various cell cultures and demonstrated efficacy in rodents and nonhuman primates, there were observed instances of cell death at higher concentrations and with prolonged exposure.[19] These limitations could be effectively addressed by fine-tuning the synthesis process in a more suitable clinical buffer such as saline or phosphate-buffered saline (PBS).

On the other hand, considerable attention has been focused on cancer theranostics involving gases due to their notable therapeutic efficacy and favorable biosafety profile.[22] For instance, the effectiveness of radiotherapy in treating solid tumors faces limitations due to the presence of hypoxic microenvironments ($pO_2 \leq 2.5$ mmHg).[23,24] This is attributed to excessive oxygen consumption by rapidly multiplying cancer cells and abnormal vasculature, which restricts oxygen supply to the interior regions of the tumors. Consequently, these areas become resistant to radiotherapy, where oxygen plays a crucial role in enhancing radiation-induced cell damage. To mitigate hypoxia and improve the effectiveness of the treatment, the reoxygenation of the tumor proves to be an efficient approach. Three primary strategies have been documented for achieving tumor oxygenation: (i) the direct or indirect delivery of O_2 into the tumor using nanocarriers, (ii) the in situ catalytic decomposition of H_2O_2, and (iii) the in situ splitting of water.[22] Indeed, the ability of zeolite nanocrystals to release gases as carbogen, a mixture comprising 95% O_2 and 5% CO_2, has been demonstrated within brain tumors.[19]

In this study, we have developed a novel synthesis strategy to prepare an injectable suspension of zeolite nanocrystals directly in a physiological solution, specifically focusing on their potential applications in addressing hypoxia, a prominent characteristic of most solid tumors. Additionally, we strategically introduced gadolinium into the zeolite nanocrystals to facilitate their localization within tissues. This incorporation of gadolinium enabled us to track the zeolite nanocrystals with MRI and discern the regions of their distribution. Our research delves into a comprehensively study of the structure, morphology, toxicity, and, most importantly, the gas storage and delivery properties of the FAU zeolites. This endeavor aims to significantly contribute to advancing treatment strategies, ultimately leading to improved outcomes in cancer therapy.

EXPERIMENTAL SECTION

Synthesis of Nanosized FAU Zeolite. Sodium hydroxide pellets (NaOH, 98%), colloidal silica (Ludox HS30), and gadolinium nitrate hexahydrate $Gd(NO_3)_3{\cdot}6H_2O$ (99.99%) were purchased from Sigma-Aldrich. Aluminum powder (325 mesh, 99.5%) was purchased from Alfa Aesar. All reagents were used as received without further purification. Phosphate-buffered saline (PBS, 1×), which was purchased from Sigma-Aldrich was used as the solvent for all syntheses.

The FAU nanosized zeolite was synthesized under hydrothermal conditions with the molar composition of the precursor suspension: 8.3 Na_2O:10 SiO_2:1.1 Al_2O_3:55.6 PBS. The PBS solution is composed of 0.137 M NaCl, 0.27 M KCl, 10 mM Na_2HPO_4, and 1.8 mM KH_2PO_4 in sterilized water.

Sodium hydroxide (2.3 g) was dissolved in 3 mL of PBS solution, followed by the slow addition of 0.29 g of aluminum powder to form solution A. In parallel, colloidal silica (10 g) was dissolved in the alkali solution of PBS, which contained 1.1 g of NaOH and 1 g of PBS, to form clear solution B. Solution B was then added dropwise to solution A, which was kept in an ice bath under rapid stirring. The resulting mixture was aged for 24 h. After the aging process, 6 g of water was removed from the mixture through freeze-drying before subjecting it to hydrothermal treatment at 50 °C for 25 h. The colloidal FAU nanocrystals (2.5 wt %) were purified with PBS using membrane dialysis until a pH of 7.4 was reached.

The sample prepared in PBS was referred to as PBS-Na-FAU. For comparison, a sample was prepared in water following the same procedure, but water, instead of PBS, was used; the sample was referred to as ref-Na-FAU.

The as-synthesized nanosized zeolites (PBS-Na-FAU and ref-Na-FAU) were ion-exchanged using 0.3 mM of $Gd(NO_3)_3{\cdot}6H_2O$ solution as described elsewhere.[25] The resulting Gd-exchanged FAU zeolite was purified and redispersed in PBS buffer. The samples prepared in PBS and water and exchanged with Gd are referred to as PBS-Gd-FAU and ref-Gd-FAU, respectively.

Suspensions of PBS-Na-FAU and PBS-Gd-FAU zeolites (2.5 wt %) were prepared by dispersing the zeolites in PBS. Each 5 mL suspension was transferred into a 50 mL bottle sealed with a rubber plug. To achieve oxygen saturation, the suspensions were then bubbled with oxygen at a flow rate of 1 L/min for at least 30 min. The samples loaded with oxygen were abbreviated as PBS-Na-FAU@O_2 and PBS-Gd-FAU@O_2. Additionally, the samples loaded with carbogen (95% O_2 and 5% CO_2) were abbreviated as PBS-Na-FAU@Carbogen and PBS-Gd-FAU@Carbogen and compared with the reference sample PBS@Carbogen.

Characterization. The powder X-ray diffraction measurements of the samples were performed on a PANalytical X'Pert Pro diffractometer using Cu Kα1 radiation (λ = 1.5406 Å, 45 kV, 40 mA).

Magic-angle spinning nuclear magnetic resonance (MAS NMR) experiments of zeolite samples were recorded with a single pulse on a Bruker Avance 500 MHz (11.7 T) spectrometer using a 4 mm OD zirconia rotor with a spinning frequency of 12 kHz.

Raman spectra were collected using a Horiba Jobin Yvon HR Evolution spectrometer equipped with a microscope (100× objective) and a CCD detector. A 532 nm wavelength laser was used; each spectrum was accumulated four times for 30 s.

The chemical composition of the samples was determined with inductively coupled plasma mass spectrometry (ICP-MS) using a 7900 ICP-MS instrument from Agilent Technologies.

The average size of particles synthesized in PBS was determined by dynamic light scattering (DLS) using a Malvern Zetasizer Nano instrument. The surface charge of the samples was measured by conducting ζ potential measurements on the same suspensions.

The scanning electron microscopy (SEM) and energy-dispersive X-ray (EDX) spectroscopy were performed with a Tescan Mira I LMH under 20 kV. The morphology and size of nanoparticles were studied by high-resolution transmission electron microscopy (HRTEM) imaging with an FEI Tecnai G2 30 microscope (Vacc = 300 kV, LaB6).

Nitrogen adsorption−desorption isotherms were measured at −196 °C using a Micromeritics 3Flex Surface Characterization unit. The surface area was determined using the Brunauer−Emmett−Teller (BET) method, while the micropore volume was determined using the α-plot method. Additionally, O_2, CO_2, and N_2 adsorption isotherms were measured at 0, 25, and 37 °C, respectively, in the pressure range of 0−100 kPa. Prior to analysis, all samples were degassed at 250 °C under a vacuum overnight.

The thermal stability of samples was investigated through thermogravimetric analysis (TGA) using a TAG24 SETARAM analyzer under a 40 mL/min airflow. The measurements were carried out between 25 and 800 °C, with a heating rate of 10 °C/min.

Fourier transform infrared (FTIR) spectra were recorded in the mid-IR region (4000−400 cm^{-1}) using a Nicolet Nexus FTIR spectrometer at an optical resolution of 4 cm^{-1} with 64 scans. The samples were pressed into self-supported disks with a radius of 1.6 cm and a weight of 20 mg. The disks were outgassed at 0.13 kPa at 400 °C for 2 h (heating rate of 5 K/min). The amount of adsorbed gases was controlled by two pressure transducers, which measured the pressure of (i) the entire line and (ii) the gas aliquots in the calibrated volume before they were admitted into the cell. The temperature of the sample was monitored during the treatment by using a thermocouple inserted into the heater compartment of the cell. The adsorption of $^{16}O_2$ and $^{18}O_2$ gases was followed by in situ FTIR

https://doi.org/10.1021/acsami.4c20383
ACS Appl. Mater. Interfaces XXXX, XXX, XXX−XXX

spectroscopy. The peak area at 1553 and 1465 cm^{-1}, corresponding to $^{16}O_2$ and $^{18}O_2$, respectively, was measured.

Cell Culture and Cell Viability. The human glioblastoma-derived cell line U87-MG (Cellosaurus_0022), purchased from the American Type Culture Collection (ATCC), was cultured in Dulbecco's modified Eagle's medium (DMEM) containing 1 g/L of glucose (Sigma-Aldrich), supplemented with 10% fetal calf serum (Eurobio), 2 mM L-glutamine (Sigma-Aldrich), 100 U/mL penicillin, and 100 μg/mL streptomycin (Sigma-Aldrich). The cell line was maintained in culture at 37 °C with 5% CO_2 and 95% humidity. Cell viability analyses were performed under exposure to increased concentrations of reference and freshly synthesized nanosized zeolites for 72 h using a WST-1 assay (Roche) according to the manufacturer's instructions.

Hemolysis Assay. The red blood cells (RBCs) were collected from fresh rat blood by centrifugation (1000 rpm for 5 min) and suspended in PBS solution. Then, freshly synthesized reference and PBS-Na-FAU and PBS-Gd-FAU nanoparticles at increasing concentrations were incubated with 500 μL of an RBC suspension. Saline and 1% Triton X-100 were used as negative and positive controls, respectively. After incubation at 37 °C for 1 h, the samples were centrifuged (2000 rpm, 10 min), and the absorption of each supernatant at 540 nm was analyzed by a spectrophotometer (Spark, TECAN, Männedorf, Switzerland). Hemolysis of RBCs was calculated as a percentage, according to eq 1:

$$\text{hemolysis (\%)} = \frac{\text{sample absorbance} - \text{negative control absorbance}}{\text{positive control absorbance} - \text{negative control absorbance}} \times 100 \quad (1)$$

Analysis of Oxygen Release Using Nanozeolites. The oxygen release capacity of PBS-Na-FAU@O_2 and PBS-Gd-FAU@O_2 nanozeolites in aqueous solution was studied in a hypoxia workstation (InvivO2 500, Baker Ruskinn, Alliance Bio Expertise) set at 0.1% O_2 and 5% CO_2 at 37 °C in a humidified atmosphere, as previously reported. A closed reaction tube containing 12 mL of equilibrated PBS at 0.1% O_2 and 37 °C was used, and a dissolved oxygen sensor (SevenGo (Duo) pro/OptiOx, Mettler Toledo) was immersed in the PBS solution. Before the experiments, the baseline was established by measuring the oxygen saturation in the PBS solution for 30 min. Oxygen-saturated nanosized PBS-Na-FAU@O_2 and PBS-Gd-FAU@O_2 zeolites (500 μL at 1 wt %) were then added to the system. The oxygen dissolved in the PBS solution was measured for 60 min. The oxygen release capacity of the nanosized zeolite samples was compared to oxygen-saturated pure PBS (used as a control).

Relaxometry Measurements. PBS-Gd-FAU samples with a concentration ranging from 0.18 to 0.001 mM Gd were used. Solutions were placed in polypropylene tubes set on a polystyrene support. MRI acquisitions of the phantoms were performed at room temperature on a hybrid PET/7 T MRI system (Bruker, Ettlingen, Germany). For $T1$-weighted ($T1$w) images, a flow-sensitive alternating inversion recovery and rapid acquisition with relaxation enhancement (FAIR-RARE) sequence was used (TR = 6000 ms; TE = 77.82 ms; TI: increasing from 25 to 5000 ms; RARE factor of 32; image matrix: 128 × 128; 1 slice with a thickness of 3 mm; acquisition time = 4 min). Image analysis and $T1$ calculations were performed with Bruker Paravision (version 360.3.3) and MATLAB R2021b using a Levenberg–Marquardt algorithm. The $R1$ value ($1/T1$) was plotted as a function of the Gd concentration, and the slope of the line corresponded to the relaxivity ($mM^{-1}{\cdot}s^{-1}$). In this study, 1 mM Dotarem, water, and pure PBS were used as control samples.

Animal Studies. Animal investigations were performed in accordance with the European directive (2010/63/EU) and approved by the ethical committee (CENOMEXA) and the French Ministère de l'Enseignement Supérieur, de la Recherche et de l'Innovation with the authorization APAFIS#12727.

Biocompatibility of PBS-Gd-FAU *In Vivo*. PBS-Gd-FAU zeolite suspensions were injected into the tail vein of healthy nude male rats (250–350 g, CURB, Caen, France) at a dose of 10 mg/kg. A saline solution was injected as a control. Analyses were performed 48 h postadministration.

Blood Analysis. A blood sample (300 μL) was collected in an ethylenediaminetetraacetic acid (EDTA)-treated tube for complete blood count (CBC), performed at LABÉO (Frank Duncombe Laboratories, Saint-Contest, France).

Histological Analysis–Hematoxylin–Eosin Staining. At the end of the experiments, rats were painkilled with buprenorphine (Buprecare, 0.05 mg/kg, SC), deeply anesthetized, and then transcardially perfused with cold heparinized saline solution. The main organs (brain, kidney, liver, lung, and spleen) were retrieved, immediately snap-frozen in *n*-pentane (Sigma-Aldrich), and stored at −80 °C before processing. Thereafter, organs were cut with a cryostat to obtain sections of 20 μm collected on superfrost slides (Thermo Fisher Scientific). Tissue sections were postfixed 20 min in 4% paraformaldehyde (Sigma-Aldrich), washed in PBS (2 × 1 min), and soaked in hematoxylin solution (modified Harris hematoxylin, Thermo Fisher Scientific) for 4 min. The tissue sections were washed using tap water (2 × 30 s), blued in Scott's water substitute (1 min), and rinsed using water again (2 × 1 min). Tissue sections were then dehydrated in 95% alcohol (30 s) before being soaked in eosin solution (eosin-Y alcoholic, Thermo Fisher Scientific) for 2 min, then dehydrated in 100% alcohol (2 × 1 min). Tissue sections were dipped in toluene (Sigma-Aldrich) for 1 min and coverslipped with Eukitt quick-hardening mounting medium (Sigma-Aldrich). Slices were then acquired at 20× magnification with an epifluorescence microscope (Leica DMi8S, Leitz Leica, Wetzlar, Germany) equipped with a Leica DFC450 camera controlled by MetaMorph software (version 7.8.13.0, Molecular Devices). Images were analyzed using ImageJ software (version 1.50f).

Glioblastoma Multiforme (GBM) Model. Six-week-old nude male and female rats (250–350 g, CURB, Caen) were used for the study. Rats were housed at the specific-pathogen-free ONCOModels platform (CYCERON, Caen, France). Rats were anesthetized with 5% isoflurane for induction and 2% during surgery in a mixture of 70% N_2O and 30% O_2. Prior to surgery, animals were given Buprecare (0.05 mg/kg, subcutaneously) for pain relief. The depth of anesthesia was assessed beforehand by foot reflex. Subsequently, the rats were placed in a stereotactic frame after the application of xylocaine gel to the ear bars. A burr hole with a diameter of 1 mm was drilled into the skull at coordinates 3 mm lateral, 0 mm anteroposterior, and 6 mm depth from the Bregma reference point. U87-MG cells (5×10^4 cells in 3 μL PBS-glutamine 2 mM) were injected into the striatum using a dental needle (30G; 0.3 × 23 mm^2) at a flow rate of 0.6 μL/min for 5 min. The needle was withdrawn after 5 min to prevent cell reflux. Upon completing the procedure, the animals were sutured and given pain relief 6 and 24 h post-surgery.

Magnetic Resonance Imaging Studies. MRI acquisitions were performed on a hybrid PET/7 T MRI system (Bruker) with the rats under anesthesia (5% isoflurane for induction and 2% for maintenance, in a mixture of 70% N_2O and 30% O_2) and placed in a prone position. After a localizer image, an anatomical exploration of the brain was performed using a $T2$-weighted sequence to monitor tumor development (RARE with acceleration factor of 8; TR = 5000 ms; TE = 16.25 ms; experiment average = 1; 20 contiguous slices; field of view (FOV): 38.4 × 38.4 × 15; matrix: 256 × 256 × 20; resolution: 0.150 × 0.150 × 0.75; acquisition time = 2 min). TR and TE are repetition time and echo time, respectively. In order to track the brain distribution of PBS-Gd-FAU nanosized zeolites, $T1$-weighted-FLASH images (TR = 122 ms; TE = 4 ms; experiment average = 1; experiment repetition = 20; 20 contiguous slices; field of view (FOV): 35 × 35 × 15; matrix: 192 × 192 × 10; resolution: 0.182 × 0.182 × 1.50; acquisition time = 7 min 30 s) were acquired before and after caudal intravenous injection of 10 mg/L of PBS-Gd-FAU zeolite suspension (250–350 μL at 1 wt %) in tumor-bearing rats. In this study, a healthy contralateral brain was used as a control. Image analysis was performed with ImageJ software (version 1.50).

Gas release from zeolites was assessed by quantifying the fractional cerebral blood volume (fCBV). Before injecting the contrast agent, $T2$*-weighted images (TR = 20,000 ms; TE = 14 ms; experiment average = 1; 10 contiguous slices; field of view (FOV): 31.5 × 25 × 15; matrix: 100 × 80 × 50; resolution: 0.315 × 0.312 × 0.3;

https://doi.org/10.1021/acsami.4c20383
ACS Appl. Mater. Interfaces XXXX, XXX, XXX–XXX

acquisition time = 3 min 20 s) were acquired. 2 min after the injection of P904 (200 μmol/kg, Guerbet), a second *T*2w scan was acquired to establish baseline prior to an intravenous injection of carbogen-saturated PBS-Gd-FAU (10 mg/L; at least 30 min at 1 L/min; called PBS-Gd-FAU@Carbogen), followed by *T*2w scans every 5 min for 20 min. CBV maps (expressed as a percentage) were computed as previously described.[18] In this study, carbogen-saturated PBS (PBS@Carbogen) was employed as a control.

Statistical Analysis. Statistical analyses were performed with GraphPad Prism software (version 10.2.3). Data are presented as mean values ± the standard deviation (SD). The tests and the number of experiments performed are detailed in each figure legend.

RESULTS AND DISCUSSION

Synthesis, Characterization, and Colloidal Stability of Zeolite Suspensions. The new synthesis strategy involves the utilization of PBS as the solvent medium for synthesizing biocompatible nanosized zeolite particles. The effect of cations and anions within PBS is expected to impact the zeolite synthesis process. Therefore, the crystallization process of two samples, PBS-Na-FAU and ref-Na-FAU, was systematically examined by recording the powder X-ray diffraction (PXRD) patterns of samples subjected to different crystallization times (Figure S1). Initially, both samples exhibited an amorphous nature, as shown by X-ray diffraction (XRD) (Figure S1a,b). The first Bragg peaks corresponding to the FAU zeolite appeared after 6 h in both systems. As the synthesis progressed, the crystallinity of the samples gradually increased and fully crystalline materials were obtained after 25 h. Prolonged synthesis time resulted in a decrease in the crystallinity of the samples, attributed to the partial dissolution of FAU crystals, leading to the formation of the more thermodynamically stable and denser sodalite (SOD) phase. The same tendency was observed in both samples; however, this process was first observed in sample ref-Na-FAU (Figure S1b). Both PBS-Na-FAU and ref-Na-FAU samples with high crystallinity were obtained after 25 h (Figure 1). The broad Bragg peaks indicate the formation of zeolite crystals with nanosized dimensions.

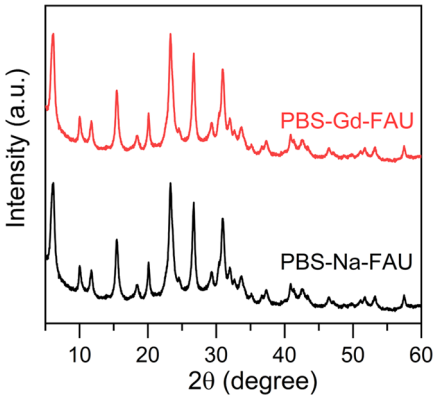

Figure 1. XRD patterns of nanosized zeolite samples synthesized in PBS buffer before (PBS-Na-FAU) and after gadolinium exchange (PBS-Gd-FAU).

MRI is an advanced imaging technique in biomedical research and clinical diagnosis, due to its non-invasive detection, superior spatial resolution, deep tissue penetration, and avoidance of radiation damage.[26] Gadolinium-based contrast agents play a crucial role in clinical MRI by enhancing the visibility of tissues and detecting lesions. Gd^{3+} ions, known for their large number of unpaired electrons and long electron spin relaxation time, effectively promote longitudinal proton relaxations.[26−28] To advance MRI contrast agents, we integrated gadolinium as extraframework cations in the FAU zeolite structure *via* ion exchange (sample PBS-Gd-FAU). This approach creates an efficient and effective gadolinium-based contrast agent, potentially leading to improved diagnostic capabilities in medical imaging. The PXRD patterns, as shown in Figure 1, demonstrated that the FAU zeolite subjected to gadolinium ion exchange preserved its high crystallinity.

The Raman spectra of the PBS-Na-FAU and PBS-Gd-FAU samples (Figure 2) show significant structural changes

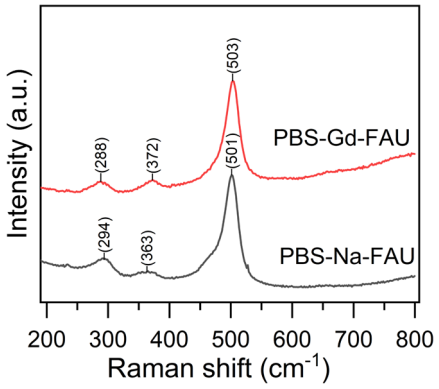

Figure 2. Raman spectra of PBS-Na-FAU and PBS-Gd-FAU nanosized zeolites.

following the exchange of Na^+ with Gd^{3+} ions. The most intense band, attributed to the vibration of four-membered rings, appears at 501 cm^{-1} in the spectrum of sample PBS-Na-FAU and shifts slightly to 503 cm^{-1} in the spectrum of PBS-Gd-FAU.[29,30] This shift may be due to the hydration and dehydration processes accompanying the migration of Gd^{3+} ions, resulting in local framework distortions. Additional bands in the lower-frequency region, such as those at 294 and 363 cm^{-1} for PBS-Na-FAU, are attributed to the vibrations of six-membered rings.[31] Notably, the band at 363 cm^{-1} is also assignable to the rocking mode of H_2O, a characteristic commonly observed for water adsorbed within zeolite pores.[32,33] These bands shift and change in intensity after the exchange process. The substitution of Na^+ with Gd^{3+} is presumed to modify the degree of ring deformation, contributing to variations in the band intensity.

The ^{29}Si and ^{27}Al NMR spectra of PBS-Na-FAU and PBS-Gd-FAU are presented in Figure 3a,c. The ^{29}Si NMR spectra of both zeolite samples exhibit peaks at −86, −89, −95, −99, and −103 ppm, corresponding to the $Q^0(4Al)$, $Q^1(3Al)$, $Q^2(2Al)$, $Q^3(1Al)$, and $Q^4(0Al)$ silicon species, respectively. In the ^{27}Al NMR spectra (Figure 3b,d), the peak at 62 ppm observed in both PBS-Na-FAU and PBS-Gd-FAU is attributed to aluminum in a tetrahedral coordination within the FAU-type zeolite framework.

Scanning electron microscopy (SEM) and transmission electron microscopy (TEM) analyses were employed to examine the morphology and size of the synthesized zeolite crystals. Both PBS-Na-FAU and PBS-Gd-FAU samples exhibit spherical morphology, with an average particle size of 30−40 nm (Figure 4a,b). The ion exchange process did not induce any changes in the size or morphology of the crystals. Well-defined nanocrystals with a high degree of crystallinity,

https://doi.org/10.1021/acsami.4c20383
ACS Appl. Mater. Interfaces XXXX, XXX, XXX−XXX

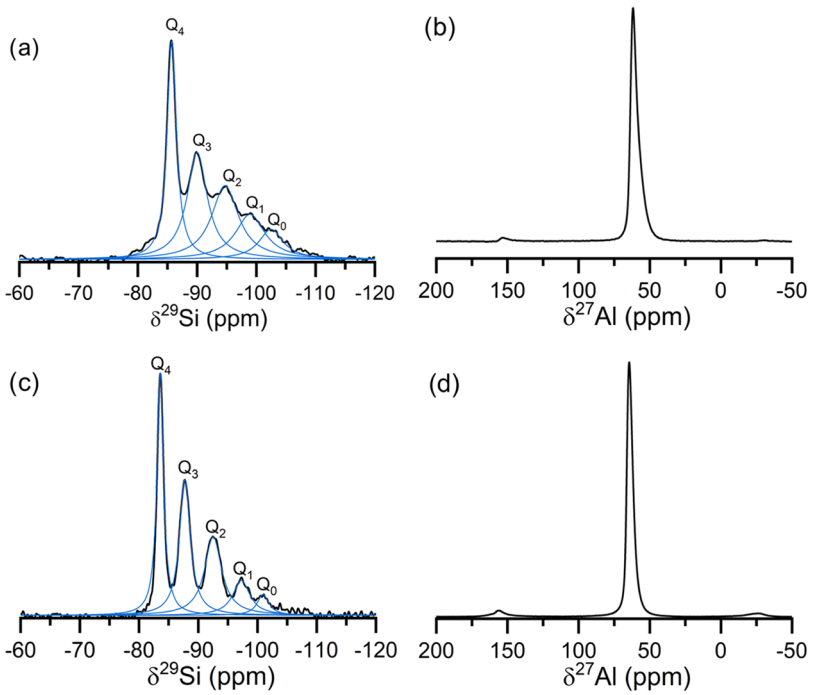

Figure 3. (a) ^{29}Si and (b) ^{27}Al MAS NMR spectra of PBS-Na-FAU, (c) ^{29}Si and (d) ^{27}Al MAS NMR spectra of the PBS-Gd-FAU nanosized zeolite samples.

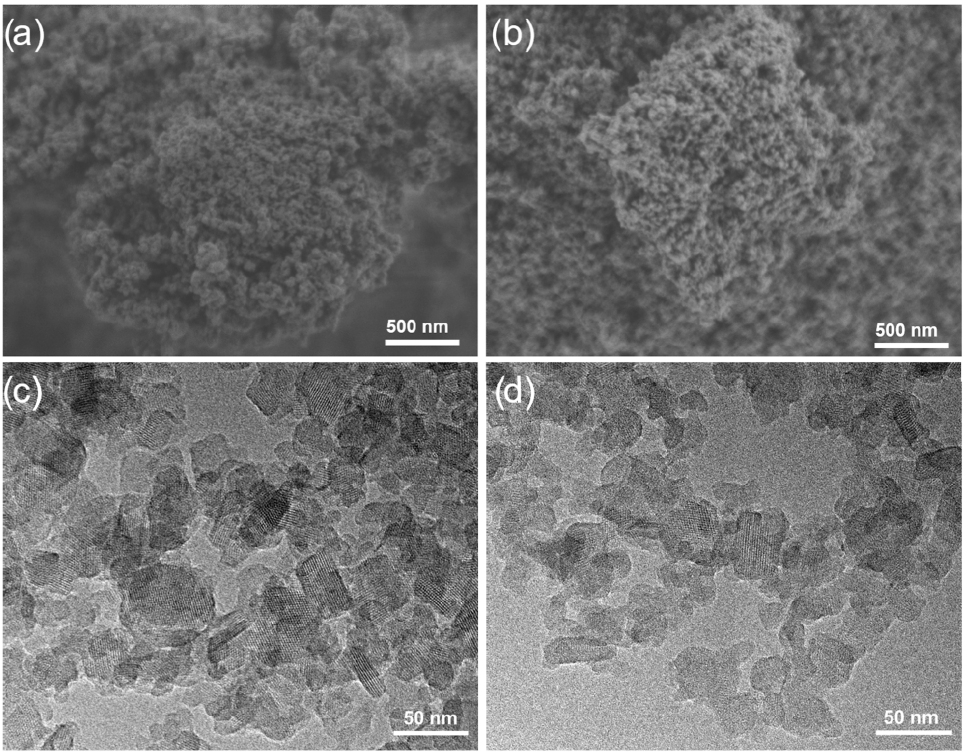

Figure 4. SEM images of (a) PBS-Na-FAU and (b) PBS-Gd-FAU nanosized zeolites synthesized in PBS, with corresponding TEM images shown in parts (c) and (d), respectively.

confirmed by the presence of fringes, are observed in Figure 4c,d.

The stability of the PBS-Na-FAU sample in PBS buffer at a physiological pH of 7.4 was assessed by examining changes in the UV−visible spectra. In addition, the mean hydrodynamic diameter of the zeolite nanocrystals was measured by DLS over time. The absorbance profile (Figure 5a) showed no variation, even after 1 week, suggesting no sedimentation of zeolite nanocrystals. Figure S2 shows the DLS profiles of PBS-Na-FAU and PBS-Gd-FAU zeolite suspensions in PBS at a physiological pH of 7.4. The mean hydrodynamic diameter of zeolite crystals in samples PBS-Na-FAU and PBS-Gd-FAU is

https://doi.org/10.1021/acsami.4c20383
ACS Appl. Mater. Interfaces XXXX, XXX, XXX−XXX

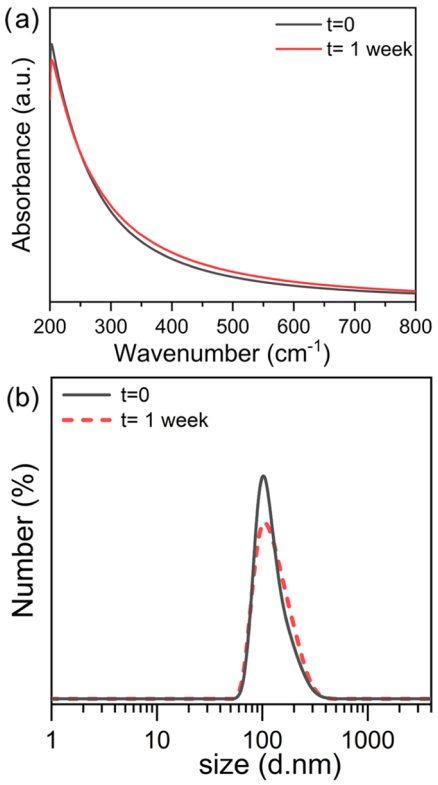

Figure 5. (a) UV−visible spectra and (b) DLS curves of sample PBS-Na-FAU measured after the preparation and after 1 week of aging at ambient conditions.

60 nm. In contrast, the mean particle size of the reference sample, ref-Na-FAU in a water suspension, is about 35 nm. The larger particles measured in PBS-Na-FAU and PBS-Gd-FAU suspensions are explained by the reversible particle aggregation resulting from the increased ionic strength in the PBS solution. No variations were detected in the mean hydrodynamic diameter of the nanoparticles (Figure 5b), indicating stable suspensions. Additionally, the colloidal stabilization of nanoparticles dispersed in PBS solution appears stable for up to 1 month without noticeable sedimentation, as shown in Figure 6. This indicates that no particle aggregation occurred over time. This result was further supported by the highly negative values of the ζ potential values measured. The ζ potential values (Figure S3a,b) readings for PBS-Na-FAU and PBS-Gd-FAU zeolite samples are −25 and −28 mV, respectively, demonstrating the colloidal stability of both suspensions.

The thermogravimetric analysis (TGA) results for the as-synthesized PBS-Na-FAU and PBS-Gd-FAU are depicted in Figure S4. Both samples exhibit a weight loss in the temperature range between 30 and 250 °C, which corresponds to the removal of physically adsorbed water from the zeolite structure. The total water content in both samples is approximately 25%. Importantly, the ion exchange process did not alter the hydrophilicity of the samples. The chemical composition of both samples, PBS-Na-FAU and PBS-Gd-FAU, was determined *via* EDX spectrometry (Figure S5a,b). The EDX results confirmed the presence of Si, Al, and alkali metals (Na and K) and phosphorus (P). The presence of K and part of Na, along with P, originates from the PBS solution. After the gadolinium ion exchange process, potassium was fully exchanged, while sodium was only partially exchanged. This is attributed to the fact that sodium plays a crucial role in stabilizing the SOD cages present in the FAU structure. These results were further confirmed by ICP-MS analysis (Table 1).

Table 1. Elemental Composition of Nanosized Zeolite Samples Determined by ICP-MS

	chemical composition (wt %)					
sample	Na	K	Si	Al	Gd	Si/Al
ref-Na-FAU	11.27		16.24	12.42		1.30
PBS-Na-FAU	8.33	1.23	17.96	9.33		1.85
PBS-Gd-FAU	7.95	0.48	18.36	9.61	2.03	1.84

The stoichiometric chemical composition and Si/Al molar ratio of the samples, determined by combining the ICP-MS elemental analysis and TG results, are as follows:

sample PBS-Na-FAU: $|Na_{69.79}K_{6.06}(H_2O)_{211.85}|(Si_{123.09}Al_{66.59}O_{384})$ (Si/Al = 1.85)

sample PBS-Gd-FAU: $|Na_{63.92}K_{2.33}Gd_{2.44}(H_2O)_{165.49}|(Si_{123.26}Al_{67.13}O_{384})$ (Si/Al = 1.84)

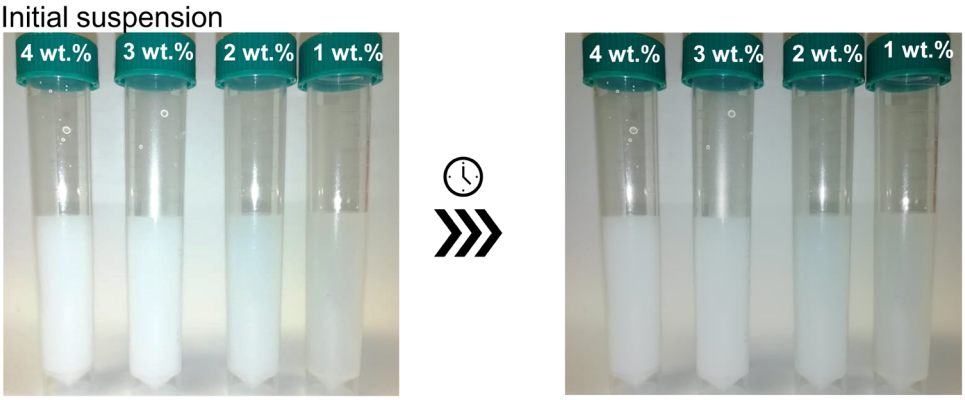

Figure 6. Representative photographs of PBS-Na-FAU suspensions with different concentrations (4, 3, 2, and 1 wt %) before and after 1 month storage at ambient conditions.

https://doi.org/10.1021/acsami.4c20383
ACS Appl. Mater. Interfaces XXXX, XXX, XXX−XXX

The Si/Al ratio slightly increased for sample PBS-Na-FAU (Si/Al = 1.85) using PBS solvent in comparison to that of ref-Na-FAU (Si/Al = 1.30) synthesized in water. This may be attributed to the ability of PBS to decrease the pH of the precursor suspension, potentially resulting in an increase in the Si/Al ratio.

The textural properties of PBS-Na-FAU and PBS-Gd-FAU samples were investigated through nitrogen adsorption−desorption measurements at −196 °C. The nitrogen adsorption isotherms are shown in Figure S6, and the textural parameters are summarized in Table 2. Both samples displayed

Table 2. Properties of PBS-Na-FAU and PBS-Gd-FAU Nanosized Zeolites

sample	surface area S_{BET} (m^2/g)	micropore surface area S_{micro} (m^2/g)	total pore volume (cm^3/g)	micropore volume (cm^3/g)
PBS-Na-FAU	704	354	0.93	0.19
PBS-Gd-FAU	494	313	0.92	0.13

mixed type I and IV isotherms according to the IUPAC classification.[34] This type of isotherm is typically observed for monodispersed nanoparticles. The agglomeration of these zeolite nanoparticles contributes to the formation of extensive interparticle mesopores. This result is consistent with the TEM observations. A decrease in the BET surface area of the ion-exchanged sample PBS-Gd-FAU was measured, while no pore blockage was observed, as the sample does not exhibit a significant decrease in the micropore volume.

Viability Assays of PBS-Na-FAU and PBS-Gd-FAU Nanosized Zeolites. To evaluate the potential of the prepared nanozeolite suspensions as sustainable materials for biomedical applications, viability assays were conducted on human glioblastoma cell lines. U87-MG cells were exposed to the ref-Na-FAU, ref-Gd-FAU, PBS-Na-FAU, and PBS-Gd-FAU zeolite samples with various concentrations for 72 h, followed by cell viability measurements. As shown in Figure 7, U87-MG cell viability decreased to 70.42 ± 7.01 and 68.92 ± 6.47% at 100 μg/mL following exposure to ref-Na-FAU and ref-Gd-FAU, respectively. Interestingly, at the highest concentrations

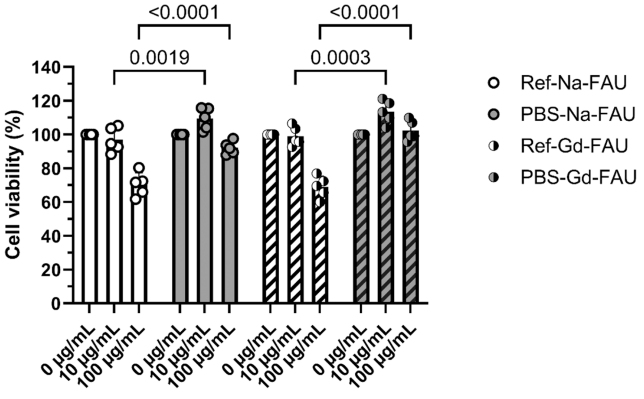

Figure 7. Cell viability of U87-MG human glioblastoma-derived cell line exposed for 72 h to increased concentrations of ref-Na-FAU, PBS-Na-FAU, ref-Gd-FAU, and PBS-Gd-FAU. Cell viability was assessed using the WST-1 assay. Mean ± SD, n = 5 independent experiments. A two-way analysis of variance (ANOVA) was performed to analyze the effect of the zeolite samples and the dose on cell viability and their interaction, followed by Tukey's test.

of PBS-Na-FAU and PBS-Gd-FAU, the U87-MG cell viability was not significantly affected, with values of 92.11 ± 3.78 and 102.26 ± 5.99%, respectively (Figure 7). These results clearly demonstrate that the nanocrystals synthesized in PBS (PBS-Na-FAU, PBS-Gd-FAU) exhibit better biocompatibility on glioblastoma cell lines compared to the reference zeolites synthesized in water (ref-Na-FAU and ref-Gd-FAU), with significant difference observed at 10 and 100 μg/mL.

As described above, one of the main advantages of working with zeolite nanocrystals synthesized in PBS is to favor their injectability and biocompatibility. To address this, we used a hemolytic assay before any *in vivo* applications. The hemolysis was calculated using eq 1, as described in the Characterization section.

The hemocompatibility of zeolites synthesized in PBS was evaluated using rat blood exposed to zeolite suspensions with increased concentrations of nanoparticles (0−500 μg/mL). As shown in Figure 8, the exposition of red blood cells with ref-

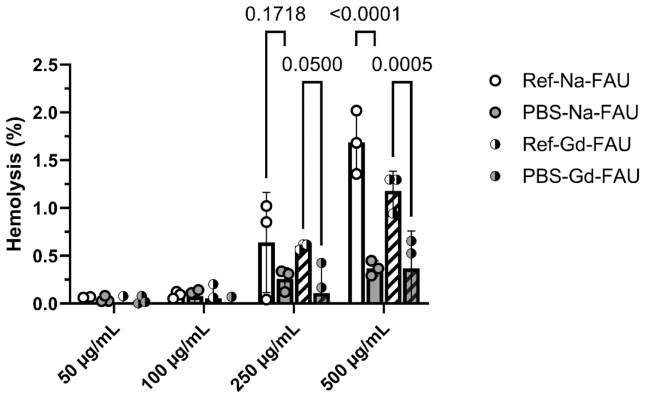

Figure 8. Hemolysis properties of ref-Na-FAU, PBS-Na-FAU, ref-Gd-FAU, and PBS-Gd-FAU nanosized zeolites incubated with RBCs at increased concentrations of 50, 100, 250, and 500 μg/mL at 37 °C for 1 h. Mean ± SD, n = 3 independent experiments, two-way ANOVA followed by Tukey's test.

Na-FAU and ref-Gd-FAU for 1 h induced a hemolytic ratio of 0.639 ± 0.524 and 0.601 ± 0.031%, respectively, at 250 μg/mL and 1.687 ± 0.331 and 1.179 ± 0.204%, respectively, at the highest concentration. Interestingly, at 250 μg/mL, compared to ref-Na-FAU and ref-Gd-FAU zeolites, the hemolytic ratio significantly decreased to 0.257 ± 0.117 and 0.110 ± 0.346% for zeolites PBS-Na-FAU and PBS-Gd-FAU, respectively. At the highest concentration of 500 μg/mL, the hemolytic ratio significantly decreased to 0.369 ± 0.078 and 0.367 ± 0.391% for samples PBS-Na-FAU and PBS-Gd-FAU, respectively (Figure 8). These results, along with *in vitro* findings, reveal an improved biocompatibility of zeolite samples synthesized in PBS (PBS-Na-FAU and PBS-Gd-FAU). However, the reference zeolite samples (ref-Na-FAU and ref-Gd-FAU) synthesized in water are considered safe according to ISO/TR7406, as the hemolysis rates of samples are less than 5%.

Biosafety Assessment of Zeolite Nanoparticles. We evaluated the potential *in vivo* toxicity of PBS-Gd-FAU zeolites by histopathological analysis with hematoxylin−eosin staining, 48 h following injection at 10 mg/kg. For further analysis, we conducted a separate study on rats to evaluate systematic toxicity through histopathological analysis of the sectioned organs: histopathological analysis with hematoxylin-eosin staining, 48 h following injection at 10 mg/kg. No apparent

https://doi.org/10.1021/acsami.4c20383
ACS Appl. Mater. Interfaces XXXX, XXX, XXX−XXX

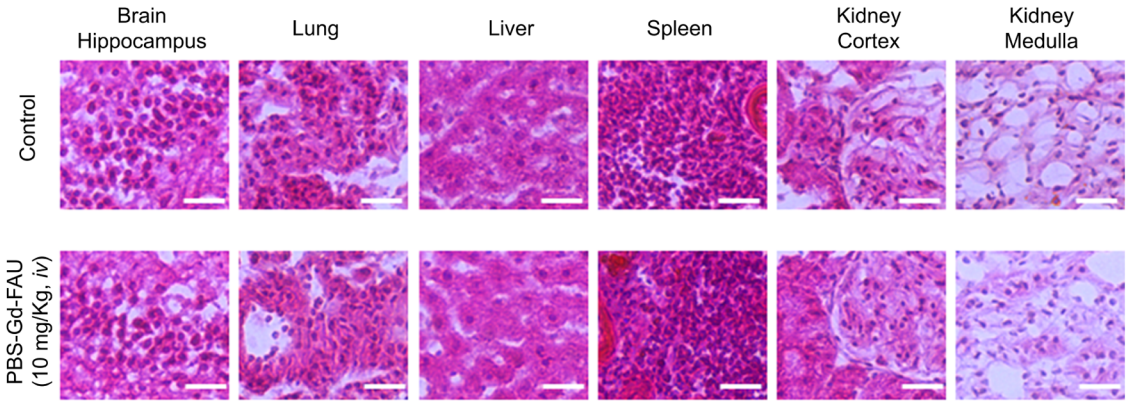

Figure 9. *In vivo* biocompatibility of PBS-Gd-FAU. Representative images of hematoxylin−eosin-stained images of major organs (brain, lung, liver, spleen, and kidney), collected 48 h after systemic administration *via* tail vein injection of PBS-Gd-FAU or saline solution at a dose of 10 mg/kg. Scale bar = 30 μm.

histopathological abnormalities in the brain, lung, liver, spleen, or kidney were observed in the PBS-Gd-FAU group compared with the control group (Figure 9). Moreover, body weight measurements and complete blood count (CBC) of the PBS-Gd-FAU-treated group were analyzed and compared with those of the saline-treated control group. Neither body weight nor hematological values were significantly altered by zeolite administration, supporting the absence of *in vivo* toxicity (Table 3).

Table 3. *In Vivo* Biocompatibility of the PBS-Gd-FAU Zeolite[a]

	48 h postinjection	
groups	control (n = 3)	PBS-Gd-FAU (10 mg/kg, iv) (n = 3)
parameters	mean ± SD	
animal's weight (g)	360.3 ± 38.5	365.6 ± 34.2
red blood cells (/mm^3)	8 686 668 ± 83 266	8 153 333 ± 342 101
leukocytes (/mm^3)	4 790 ± 1 021	5 980 ± 963
hemoglobin (g/100 mL)	15.30 ± 0.62	14.27 ± 0.65
hematocrit (%)	48.33 ± 0.76	45.97 ± 1.72
mean corpuscular rate (picog)	17.61 ± 0.57	17.50 ± 0.29
mean corpuscular volume (μ^3)	55.64 ± 0.42	56.38 ± 0.48
erythro-leukocyte ratio	1.88 ± 0.45	1.38 ± 0.15
hematocrit/hemoglobin ratio (%)	3.16 ± 0.08	3.22 ± 0.03
mean corpuscular hemoglobin concentration (%)	31.65 ± 0.80	31.03 ± 0.35
neutrophil (%)	40.63 ± 5.20	50.53 ± 8.83
eosinophil (%)	2.57 ± 0.40	3.27 ± 0.99
basophil (%)	0.37 ± 0.06	0.30 ± 0.10
monocyte (%)	5.33 ± 0.35	5.90 ± 0.46
large lymphocytes (%)	0.27 ± 0.06	0.53 ± 0.32
small lymphocytes (%)	50.83 ± 5.30	39.50 ± 9.58
platelet (/mm^3)	528 667 ± 238 475	535 000 ± 197 641
red blood cell abnormalities	none	none
leukocytes abnormalities	none	none

[a]Body weight and hematological values of nude male rats 48 h after systemic injection of PBS-Gd-FAU or saline solution (control). n = 3 animals per group. Mean ± SD, no significant differences observed according to the Mann−Whitney U Test.

Gd ions introduced in the nanosized zeolite *via* ion exchange are promising candidates as contrast agents for MRI characterization. The Gd ions shorten the longitudinal ($T1$) relaxation of protons, resulting in an increase in signal intensity and bright contrast in regions where the contrast agent accumulates in $T1$w imaging. To assess the potential of the contrast agent, the $T1$ map was plotted as a function of Gd concentration, and the $r1$ (relaxivity expressed in mM^{-1}·s^{-1}) was calculated.

Figure 10a shows grayscale-coded $T1$ maps of PBS-Gd-FAU at increased Gd concentrations (0.001−0.18 mM), demonstrating a noticeable shortening of the $T1$ values with increasing Gd concentration. The resulting $R1$ ($1/T1$) value of PBS-Gd-FAU calculated at 7 T at room temperature is 9.254 mM^{-1}·s^{-1} (Figure 10b). The calculated $r1$ value for PBS-Gd-FAU zeolite was 2 times higher than that of the commercial Gd-chelates (*e.g.*, the relaxivity induced by Dotarem Gd-DOTA is about 4 mM^{-1}·s^{-1} at 7 T).

To evaluate the biodistribution and ability of zeolites to reach tumors, the zeolite sample prepared in PBS (PBS-Gd-FAU) was injected into GBM-bearing rats at 10 mg/kg during dynamic $T1$w MRI. After intravenous injection, a hyperintense signal was observed specifically in U87-MG tumors, while no significant change was detected in the healthy brain (Figure 10c). This result confirms that the PBS-Gd-FAU zeolite nanocrystals rapidly reached the tumor, with the maximum signal observed after 90−100 s of injection (Figure 10d). However, although zeolite nanocrystals reached the tumor, $T1$w images and quantification revealed their elimination from the U87-MG tumor over time. Our results demonstrate the potential of zeolites for targeting the delivery of gases and drugs currently considered for the brain tumors.

Nanosized Zeolites as a Platform for Gas Storage and Delivery System. *Gas Adsorption Measurements: O_2, N_2, and CO_2.* The adsorption isotherms for O_2, N_2, and CO_2 on PBS-Na-FAU and PBS-Gd-FAU nanosized zeolites were measured at various temperatures and gas concentrations; the results are depicted in Figures 11a−d and S7a,b. Throughout all temperatures examined, carbon dioxide consistently exhibited the highest adsorption, followed by nitrogen, with oxygen being the least adsorbed molecule, as shown in Table 4. For instance, at 298 K, the quantities of O_2, N_2, and CO_2 adsorbed at 100 kPa on PBS-Na-FAU were found to be 0.26, 0.72, and 6.07 mmol/g, respectively. These results reveal a notable preference for carbon dioxide, aligning well with existing literature studies on other sodium-based faujasite

https://doi.org/10.1021/acsami.4c20383
ACS Appl. Mater. Interfaces XXXX, XXX, XXX−XXX

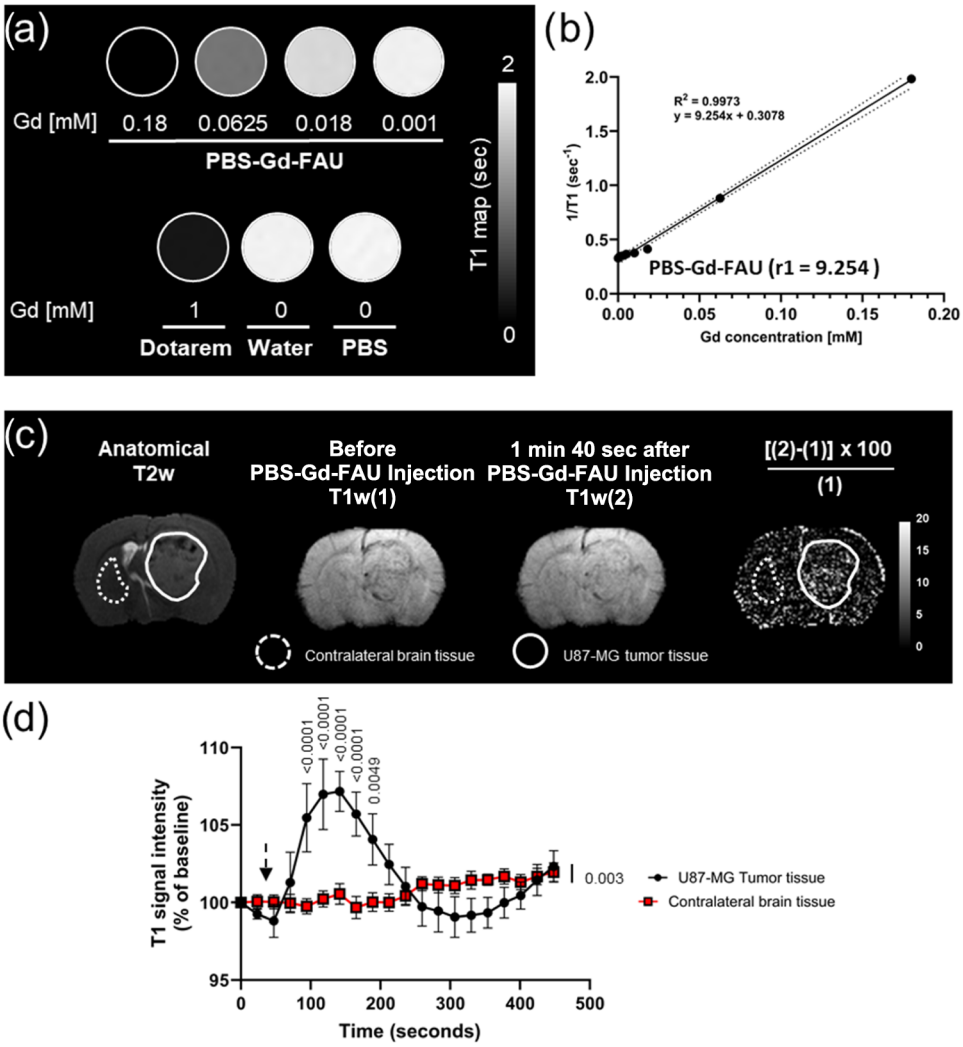

Figure 10. Distribution of PBS-Gd-FAU zeolite nanocrystals in the rat brain. (a) *T*1 maps as a function of Gd ion concentration. (b) Plots of the *R*1 value (1/*T*1) as a function of Gd ion concentration. Slope provides the relaxivity *r*1 value. (c) Representative *T*2w (anatomical) and *T*1w images acquired before (1) and 1 min 40 s after (2) intravenous administration of the PBS-Gd-FAU zeolite suspension at 10 mg/kg and map of variations between the two acquisition times. (d) Quantification of the normalized *T*1w signal intensity in the contralateral brain tissue and the U87-MG tumor tissue. Mean ± SD, n = 10 independent experiments; two-way ANOVA followed by Tukey's test.

zeolites.[35,36] The interactions between CO_2 and zeolite are facilitated by the presence of charge compensating cations within the zeolite structure as a result of the greatest ion−quadrupole interactions with CO_2.[37] The effect of charge compensating cations on the physisorption capacity for CO_2, N_2, and O_2 is presented in Table 4. Partial ion exchange of Na^+ and K^+ on FAU zeolite nanocrystals by Gd^{3+} results in a 3.26% increase in CO_2 loading (Figure 11d), while the adsorption loading for O_2 and N_2 remains relatively unchanged. Furthermore, as anticipated, the adsorption of gases diminishes with increasing temperature, highlighting the substantial impact of physical adsorption mechanisms. It is also evident that the O_2 adsorption capacity of PBS-Na-FAU is notably lower than that of N_2. This discrepancy can be attributed to the similarity in the polarization rates of the two nonpolar molecules. However, the low quadrupole moment of N_2 (1.5×10^{-26} esu·cm^2) is still higher than that of O_2 (0.4×10^{-26} esu·cm^2). This significant difference results in a stronger interaction between the electric field gradient of cations and the quadrupole moment. Consequently, the affinity of PBS-Na-FAU for N_2 surpasses that for O_2, with the interaction between the adsorbate and adsorbent playing a dominant role. The same behavior was also observed for other zeolites such as Na, Li-RHO, and Na-LTA.[38,39]

The O_2 adsorption capacity of PBS-Na-FAU zeolite was found to be twice as high compared to the reported values on micron-sized 13×, which might be attributed to the difference in crystal size.[40] The nano-PBS-Na-FAU exhibits a larger surface area, thus providing an increased number of adsorption sites.

Nature of Zeolite−Oxygen Interactions: *In Situ* FTIR Study Using Two Isotopic Forms of Oxygen $^{16}O_2$ and $^{18}O_2$. *In situ* infrared Fourier transform spectroscopy (FTIR) was used to further investigate the nature of the zeolite−O_2 interactions upon oxygen adsorption. The FTIR spectra of PBS-Na-FAU and PBS-Gd-FAU samples are similar in the silanol hydroxyl stretching range (Figure S8a,c). At 298 K and prior to O_2 adsorption, the IR spectra of both samples contain bands at 3740 and 3690 cm^{-1}, attributed to isolated internal silanol groups and hydrogen-bonded silanol groups, respectively.[41] These peaks shift to 3745 and 3695 cm^{-1} at 100 K due to the effect of the cryogenic temperature (Figure S8a,c).

https://doi.org/10.1021/acsami.4c20383
ACS Appl. Mater. Interfaces XXXX, XXX, XXX−XXX

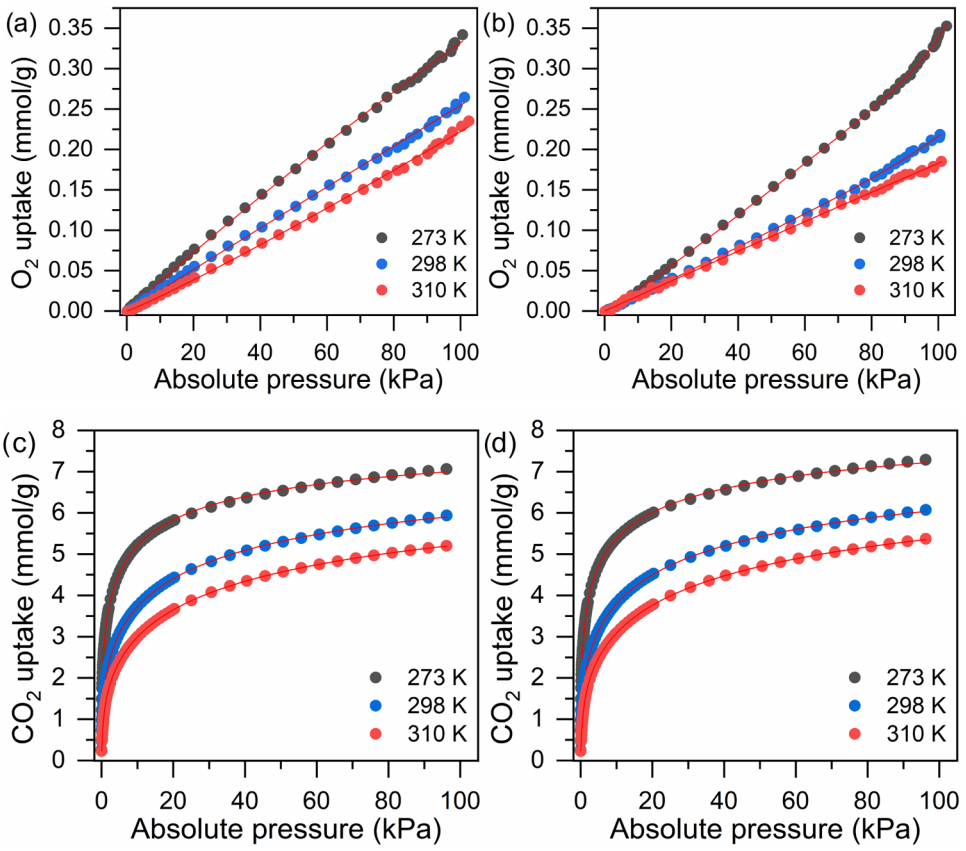

Figure 11. O_2 (a, b) and CO_2 (c, d) adsorption isotherms of PBS-Na-FAU (a–c) and PBS-Gd-FAU (b–d) nanosized zeolites at different temperatures.

Table 4. Adsorption Capacities of PBS-Na-FAU and PBS-Gd-FAU Nanosized Zeolites for O_2, N_2, and CO_2 (mmol/g) at 100 kPa

temperature (K)	O_2 (mmol/g)		N_2 (mmol/g)		CO_2 (mmol/g)	
samples	PBS-Na-FAU	PBS-Gd-FAU	PBS-Na-FAU	PBS-Gd-FAU	PBS-Na-FAU	PBS-Gd-FAU
273	0.34	0.35	0.71	0.67	7.06	7.29
298	0.26	0.22	0.39	0.39	5.94	6.07
310	0.23	0.18	0.33	0.29	5.20	5.37

Exposure of the samples to various amounts of oxygen at 100 K results in the generation of a new band in the spectrum at 1553 cm^{-1} for $^{16}O_2$ and a band at 1465 cm^{-1} for $^{18}O_2$, which are assigned to the stretching of the O═O bond adsorbed on the surface of the samples (Figure 12a). Indeed, the coordination of oxygen with the surface of zeolite disrupts the symmetry of the homonuclear diatomic molecule, making it IR active regardless of whether adsorption occurs. The shift between the bands of $^{16}O_2$ and $^{18}O_2$ is due to the difference in mass caused by the additional neutrons in oxygen-18. This mass difference alters the vibrational frequency of the O–O bond, resulting in a distinct wavenumber for each isotope, *i.e.*, $^{16}O_2$ at 1553 cm^{-1} and $^{18}O_2$ at 1465 cm^{-1}. The frequency shift of 88 cm^{-1} between $^{16}O_2$ and $^{18}O_2$ bands is expected for the free molecule, considering the mass ratio of the isotopes.

The activation of zeolites effectively dehydrated the sample. However, due to the high hydrophilic nature of the zeolite samples, rehydration occurred during the slow cooling from 673 to 273 K at 5 K/min, even under high vacuum conditions. This rehydration is indicated by the appearance of a band at 1647 cm^{-1}, associated with the bending of water (Figure S8b,d), and a band at 3199 cm^{-1}, resulting from the Fermi resonance of hydrogen bond stretching and H_2O bending (Figure S8a,c).

To ensure effective water removal, which is crucial for using FAU zeolites as adsorbents (since water occupies part of the porosity and hinders the penetration of other species under environmental conditions), a faster cooling was applied from 673 to 273 K at 30 K/min. Following this rapid cooling, the samples were immediately subjected to cryogenic conditions (100 K). The effectiveness of this treatment is demonstrated by the absence of the bands at 1647 and 3199 cm^{-1} in the FTIR spectra. Additionally, the drastic decrease of the band at 3690 cm^{-1} indicates reduced short-range silanol interactions[42] (Figure S8a,c).

In both samples, during oxygen adsorption for both isotopic forms, the vibration band corresponding to the silanol terminal hydroxyls at 3745 cm^{-1} is shifted by $\Delta\nu$ = 5 cm^{-1} and is accompanied by the appearance of a weak band at 3735 cm^{-1} (Figure 12b,c). This small shift and the formation of this band are independent of the molar amount of oxygen adsorbed, indicating a very weak interaction between the adsorbate and

https://doi.org/10.1021/acsami.4c20383
ACS Appl. Mater. Interfaces XXXX, XXX, XXX–XXX

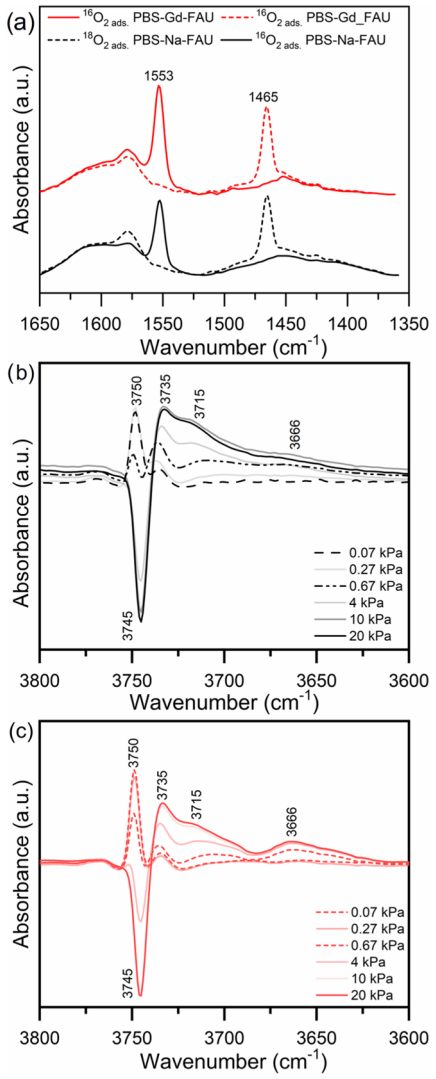

Figure 12. (a) FTIR absorption bands of $^{16}O_2$ (solid line) and $^{18}O_2$ (dotted line) after adsorption at 4 and 100 K on PBS-Na-FAU and PBS-Gd-FAU zeolite samples. Difference spectra showing the hydroxyl stretching range for (b) PBS-Na-FAU (c) and PBS-Gd-FAU during adsorption at various pressures up to 20 mbar (solid line at equilibrium pressure).

these groups. However, the decrease in silanol groups does not appear to follow a linearly the constant increase in the transition dipole moment detected by oxygen adsorption. This result indicates that the silanol sites at low concentrations of oxygen introduced into the system are not the main sites where adsorption occurs. Instead, the cationic sites of Na^+, K^+, and Gd^{3+} (for the PBS-Na-FAU and PBS-Gd-FAU samples, respectively) are primarily responsible for the adsorption.

At high oxygen loads, the shift of the terminal silanols disappears and a drastic decrease in the band at 3745 cm^{-1} is observed. Additionally, a hydrogen-bonding band at 3715 cm^{-1}, related to O_2 coordination, increases proportionally to the oxygen adsorbed into the samples analyzed.

The hydroxyl regions in the two samples are very similar, differing slightly in intensity at high oxygen concentrations and by the presence of a band at 3666 cm^{-1} (Figure 12c). This band is almost absent in the PBS-Na-FAU sample but increases proportionally with the concentration in the PBS-Gd-FAU sample. This broad band is associated with a hydrogen-bonding interaction with a longer bond length than the one appearing at 3735 cm^{-1}.

Regarding the adsorption of oxygen on the PBS-Na-FAU sample, since the sample is in the cationic form (Na^+ and K^+) and not in the H-form, it is believed that oxygen is adsorbed on the four different types of Na^+ and K^+ sites present, as described by Hattori and Ono.[43] Similar adsorption bands were observed for the PBS-Gd-FAU sample. By evaluating the changes in the normalized areas of the peaks at 1545 and 1461 cm^{-1} (Figure S9a–e) corresponding to the adsorption of $^{16}O_2$ and $^{18}O_2$, it can be noted that both samples adsorb both isotopic forms of oxygen in the same manner at a pressure in the range between 0 and 0.3 kPa (Figure 13a). This suggests

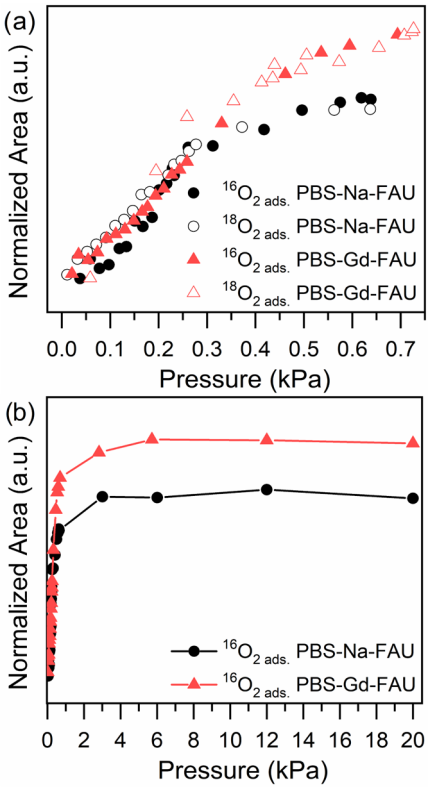

Figure 13. Weight-normalized integrated adsorption band of $^{16}O_2$ at 1553 cm^{-1} (filled symbols) and $^{18}O_2$ adsorption band at 1465 cm^{-1} (empty symbols) for the PBS-Na-FAU (black symbols) and PBS-Gd-FAU (red symbols) samples at pressures (a) 0–0.7 kPa and (b) 0–20 kPa.

that the driving force for oxygen adsorption is the same for both samples. However, the adsorption capacity differs between the two samples. Specifically, for a given amount of O_2 (both isotopic forms) introduced into the system, equal to 0.038 mmol (0.3 kPa) for the PBS-Na-FAU sample it tends to reach a plateau, while for the PBS-Gd-FAU sample, linear adsorption up to 0.5 kPa pressure is observed. The maximum areas of the two bands at 1553 and 1465 cm^{-1} are reached at a pressure of 3 kPa for PBS-Na-FAU and 6 kPa for PBS-Gd-FAU. Beyond these pressures, no further increase is observed. At an equilibrium pressure of 20 kPa, the PBS-Gd-FAU sample adsorbs approximately 23% more oxygen than the PBS-Na-FAU sample, as indicated by the difference in normalized areas (Figures 13b and S10). These differences in adsorption capacity are attributed to the introduction of a trivalent cation (Gd^{3+}) replacing three Na^+ and K^+ cations. This substitution

https://doi.org/10.1021/acsami.4c20383
ACS Appl. Mater. Interfaces XXXX, XXX, XXX–XXX

also releases additional volume, allowing the zeolite to accommodate more oxygen molecules.[25]

Oxygen Delivery by Nanosized Zeolites. The high porosity and substantial oxygen loading capacity of the PBS-Gd-FAU zeolite suggest its potential as an effective oxygen reservoir, capable of gradually releasing oxygen in oxygen-deficient environments, such as hypoxic conditions. In this experiment, we first saturated the zeolite samples with oxygen (PBS-Na-FAU@O_2 and PBS-Gd-FAU@O_2). The oxygen release concentrations were then monitored in situ by using a portable oxygen probe within a hypoxia workstation. This workstation was configured to maintain an atmosphere of 0.1% O_2 and 5% CO_2 at a constant temperature of 37 °C, with 95% relative humidity.

Immediately following the addition of PBS-Na-FAU and PBS-Gd-FAU nanozeolite suspensions into a deoxygenated PBS solution, a rapid and substantial increase in oxygen concentrations was observed (Figure 14). The pure PBS control sample showed a release of 1.23 mg/L. However, PBS does not function as an oxygen reservoir for delivering oxygen to the tumor, and instead, it is released into the bloodstream.

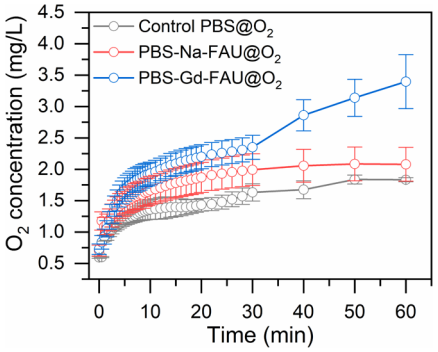

Figure 14. Time-dependent release of oxygen in PBS solution with the addition of oxygen-loaded PBS-Na-FAU@O_2 and PBS-Gd-FAU@O_2 nanosized zeolites and the oxygen-saturated PBS control sample.

The oxygen release at 30 min was measured for PBS-Na-FAU@O_2 to be 1.30 mg/L and for PBS-Gd-FAU@O_2 to be 1.64 mg/L. Subsequently, after 30 min, this concentration remained stable at 1.64 mg/L for PBS-Na-FAU and increased for PBS-Gd-FAU to 2.68 mg/L after 60 min. The PBS-Gd-FAU has the capacity to retain a higher amount of oxygen and can facilitate a slow yet continuous release of oxygen into the surrounding hypoxic environment.

To evaluate the delivery of gases (O_2 and CO_2) into tumors by PBS-Gd-FAU@Carbogen zeolites, MRI was used in the U87-MG model to study variations in CBV. These variations, measured at 10, 15, and 20 min following intravenous administration of carbogen-saturated zeolites, were quantified and indicated as ΔCBV. The results presented in Figure 15a clearly reveal a significant increase in CBV in the tumor core compared to contralateral brain tissue at 15 and 20 min after injection. Interestingly, the injection of PBS@Carbogen did not modify the CBV in the U87-MG tumor. Quantitative measurements (Figure 15b) confirmed these observations, showing variations between tumors and contralateral brain tissue of 14.91 ± 8.76 and 17.10 ± 9.14% at 15 and 20 min, respectively, following PBS-Gd-FAU@Carbogen injection, while PBS@Carbogen administration induced variations of 4.46 ± 2.88% at 15 min and 5.34 ± 3.02% at 20 min. These results demonstrate the capacity of PBS-Gd-FAU@Carbogen to release gases within the tumor, resulting in vasodilation induced by carbogen liberation, which does not occur in the surrounding tissue. Compared to our previous study with ref-Gd-FAU, the capacity for gas release seems to be significantly higher, as the difference in signal observed between healthy and tumor tissue was 5.36% after 15 min following ref-Gd-FAU zeolite administration.[19]

CONCLUSIONS

In summary, an original approach was developed for the synthesis of stable nanosized zeolite crystals directly in a clinical buffer suspension, ensuring enhanced biocompatibility. By incorporating gadolinium ions into the nanosized zeolites *via* ion exchange, an effective MRI contrast agent (sample PBS-

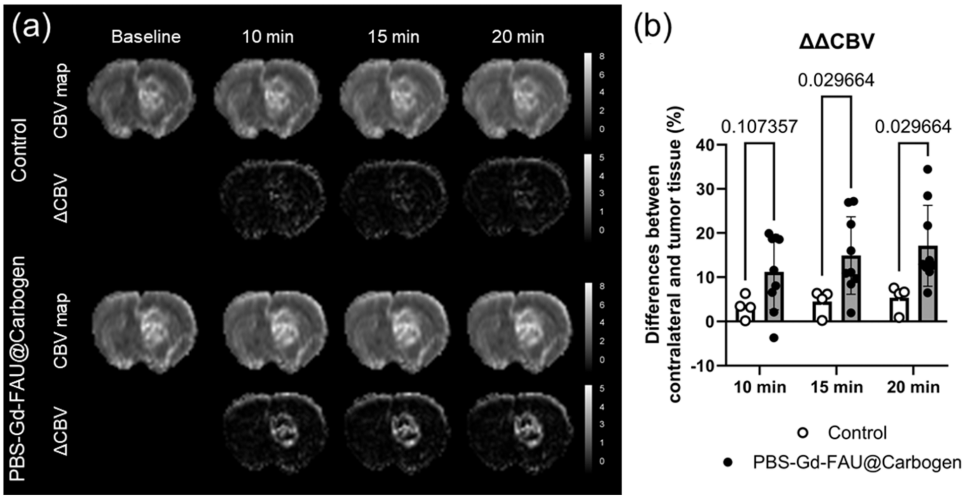

Figure 15. Gas delivery by PBS-Gd-FAU@Carbogen in brain tumor. (a) Representative CBV and ΔCBV maps obtained before and after 10, 15, and 20 min of intravenous administration of a carbogen-saturated nanosized zeolite sample (PBS-Gd-FAU@Carbogen, 10 mg/kg). The control group received an injection of carbogen-saturated PBS solution (PBS@Carbogen). (b) Quantification of the differences in ΔCBV (%) between healthy and tumor tissues (ΔΔCBV). Data are presented as mean ± SD, with n = 4 for the control group and n = 9 for the PBS-Gd-FAU@Carbogen group. Statistical analysis was performed using the Mann−Whitney U test.

https://doi.org/10.1021/acsami.4c20383
ACS Appl. Mater. Interfaces XXXX, XXX, XXX−XXX

Gd-FAU) was produced. Toxicity experiments on human glioblastoma cell lines and murine red blood cells demonstrated the nontoxic nature of both as-synthesized (PBS-Na-FAU) and gadolinium containing (PBS-Gd-FAU) nanosized zeolite particles. *In vivo* studies further showed no apparent toxicity in animal models.

The structural microporosity of these zeolites is advantageous for gas storage, allowing for the loading of significant amounts of oxygen. Notably, the PBS-Gd-FAU nanosized zeolite exhibited a remarkable oxygen release rate, reaching 2.68 mg/L in 60 min. The higher adsorption capacity of PBS-Gd-FAU is attributed to the introduction of a trivalent cation (Gd^{3+}) replacing three Na^+ and K^+ cations from the as-synthesized sample (PBS-Na-FAU). This substitution also releases additional volume, allowing the zeolite to accommodate more oxygen molecules, as demonstrated by the *in situ* FTIR study using oxygen isotopes. At an equilibrium pressure of 20 kPa, the PBS-Gd-FAU sample adsorbs approximately 23% more oxygen than the PBS-Na-FAU. The PBS-Gd-FAU@Carbogen zeolite effectively delivered oxygen and carbon dioxide specifically to brain tumor tissues, resulting in significant vasodilation, as evidenced by MRI.

Furthermore, *in vivo* MRI studies confirmed targeted delivery and gas release within the brain tumor. While the injection of the control sample (PBS@Carbogen) did not modify the CBV in the U87-MG tumor, the injection of PBS-Gd-FAU@Carbogen showed a difference between the contralateral brain tissue and tumors of 14.91 and 17.10% after 15 and 20 min, respectively. This result demonstrates the capacity of PBS-Gd-FAU@Carbogen to release gases within the tumor, resulting in vasodilation induced by carbogen liberation, which did not occur in the surrounding tissue.

Moreover, the grayscale-coded $T1$ maps of PBS-Gd-FAU showed a noticeable shortening of the $T1$ values as calculated at 7 T at room temperature of 9.254 $mM^{-1}{\cdot}s^{-1}$, which is 2 times higher than that of the commercial Gd-chelates (4 $mM^{-1}{\cdot}s^{-1}$).

These results underscore the potential of synthesizing zeolites in clinical buffers to enhance their functionality and safety for biomedical research. This advancement opens new avenues for more effective and safer cancer therapies and imaging techniques.

■ ASSOCIATED CONTENT

Supporting Information

The Supporting Information is available free of charge at https://pubs.acs.org/doi/10.1021/acsami.4c20383.

XRD patterns of samples at different crystallization times, DLS, ζ potential data, TG results, EDX data, nitrogen adsorption−desorption isotherms at 77 K, N_2 adsorption isotherms at 273 K, 298, and 310 K, and FTIR spectra (PDF)

■ AUTHOR INFORMATION

Corresponding Authors

Samuel Valable − *ISTCT UMR6030, Université de Caen Normandie, CNRS, Normandie Université, GIP CYCERON, F-14000 Caen, France*; Email: samuel.valable@cnrs.fr

Svetlana Mintova − *Université de Caen Normandie, ENSICAEN, CNRS, LCS, 14000 Caen, France*; orcid.org/0000-0002-0738-5244; Email: svetlana.mintova@ensicaen.fr

Authors

Abdallah Amedlous − *Université de Caen Normandie, ENSICAEN, CNRS, LCS, 14000 Caen, France*; orcid.org/0000-0001-8319-870X

Charly Hélaine − *ISTCT UMR6030, Université de Caen Normandie, CNRS, Normandie Université, GIP CYCERON, F-14000 Caen, France*

Francesco Dalena − *Université de Caen Normandie, ENSICAEN, CNRS, LCS, 14000 Caen, France*; orcid.org/0000-0002-6299-1626

Clément Anfray − *ISTCT UMR6030, Université de Caen Normandie, CNRS, Normandie Université, GIP CYCERON, F-14000 Caen, France*

Thomas Ménard − *Université de Caen Normandie, ENSICAEN, CNRS, LCS, 14000 Caen, France*

Isis Blanchard − *ISTCT UMR6030, Université de Caen Normandie, CNRS, Normandie Université, GIP CYCERON, F-14000 Caen, France*

Jérôme Toutain − *ISTCT UMR6030, Université de Caen Normandie, CNRS, Normandie Université, GIP CYCERON, F-14000 Caen, France*

Complete contact information is available at: https://pubs.acs.org/10.1021/acsami.4c20383

Author Contributions

[§]A.A. and C.H. contributed equally to this work.

Notes

The authors declare no competing financial interest.

■ ACKNOWLEDGMENTS

This project has received financial support from the Région Normandie through Label of Excellence for the Centre for zeolites and nanoporous materials by the Region of Normandy (CLEAR), cofunded by the European Union (ERC, ZEO-LIghT, 101054004), the European Union-Fonds Européen de Développement Régional (FEDER), the University of Caen-Normandie, Normandie Valorization (Maturation Program), the Centre National de la Recherche Scientifique (CNRS Innovation—Prematuration Program), and Institut National du Cancer (INCA-11699), all of which are acknowledged.

■ REFERENCES

(1) Moore, T. L.; Rodriguez-Lorenzo, L.; Hirsch, V.; Balog, S.; Urban, D.; Jud, C.; Rothen-Rutishauser, B.; Lattuada, M.; Petri-Fink, A. Nanoparticle Colloidal Stability in Cell Culture Media and Impact on Cellular Interactions. *Chem. Soc. Rev.* **2015**, *44* (17), 6287−6305.

(2) Etheridge, M. L.; Campbell, S. A.; Erdman, A. G.; Haynes, C. L.; Wolf, S. M.; McCullough, J. The Big Picture on Nanomedicine: The State of Investigational and Approved Nanomedicine Products. *Nanomedicine* **2013**, *9* (1), 1−14.

(3) Wagner, V.; Dullaart, A.; Bock, A. K.; Zweck, A. The Emerging Nanomedicine Landscape. *Nat. Biotechnol.* **2006**, *24* (10), 1211−1217.

(4) Farokhzad, O. C.; Langer, R. Impact of Nanotechnology on Drug Delivery. *ACS Nano* **2009**, *3* (1), 16−20.

(5) Caracciolo, G.; Pozzi, D.; Capriotti, A. L.; Cavaliere, C.; Piovesana, S.; La Barbera, G.; Amici, A.; Laganà, A. The Liposome−Protein Corona in Mice and Humans and Its Implications for in Vivo Delivery. *J. Mater. Chem. B* **2014**, *2* (42), 7419−7428.

(6) Yildiz, I.; Shukla, S.; Steinmetz, N. F. Applications of Viral Nanoparticles in Medicine. *Curr. Opin. Biotechnol.* **2011**, *22* (6), 901−908.

(7) Mitchell, M. J.; Billingsley, M. M.; Haley, R. M.; Wechsler, M. E.; Peppas, N. A.; Langer, R. Engineering Precision Nanoparticles for Drug Delivery. *Nat. Rev. Drug Discovery* **2021**, *20* (2), 101−124.
(8) Oh, I. h.; Min, H. S.; Li, L.; Tran, T. H.; Lee, Y. k.; Kwon, I. C.; Choi, K.; Kim, K.; Huh, K. M. Cancer Cell-Specific Photoactivity of Pheophorbide a—Glycol Chitosan Nanoparticles for Photodynamic Therapy in Tumor-Bearing Mice. *Biomaterials* **2013**, *34* (27), 6454−6463.
(9) Burgess, P.; Hutt, P. B.; Farokhzad, O. C.; Langer, R.; Minick, S.; Zale, S. On Firm Ground: IP Protection of Therapeutic Nanoparticles. *Nat. Biotechnol.* **2010**, *28* (12), 1267−1270.
(10) Boer, D. G.; Langerak, J.; Pescarmona, P. P. Zeolites as Selective Adsorbents for CO_2 Separation. *ACS Appl. Energy Mater.* **2023**, *6* (5), 2634−2656.
(11) Wang, T.; Chu, Y.; Li, X.; Liu, Y.; Luo, H.; Zhou, D.; Deng, F.; Song, X.; Lu, G.; Yu, J. Zeolites as a Class of Semiconductors for High-Performance Electrically Transduced Sensing. *J. Am. Chem. Soc.* **2023**, *145* (9), 5342−5352.
(12) Larsen, S. C. Nanocrystalline Zeolites and Zeolite Structures: Synthesis, Characterization, and Applications. *J. Phys. Chem. C* **2007**, *111* (50), 18464−18474.
(13) Zhang, X.; Lv, J.; Liu, J.; Xu, S.; Sun, J.; Wang, L.; Xu, L.; Mintova, S.; Song, H.; Dong, B. Stable EMT Type Zeolite/CsPbBr3 Perovskite Quantum Dot Nanocomposites for Highly Sensitive Humidity Sensors. *J. Colloid Interface Sci.* **2022**, *616*, 921−928.
(14) Mintova, S.; Jaber, M.; Valtchev, V. Nanosized Microporous Crystals: Emerging Applications. *Chem. Soc. Rev.* **2015**, *44* (20), 7207−7233.
(15) Awala, H.; Gilson, J.-P.; Retoux, R.; Boullay, P.; Goupil, J.-M.; Valtchev, V.; Mintova, S. Template-Free Nanosized Faujasite-Type Zeolites. *Nat. Mater.* **2015**, *14* (4), 447−451.
(16) Ng, E.-P.; Chateigner, D.; Bein, T.; Valtchev, V.; Mintova, S. Capturing Ultrasmall EMT Zeolite from Template-Free Systems. *Science* **2012**, *335* (6064), 70−73.
(17) Amedlous, A.; Hélaine, C.; Guillet-Nicolas, R.; Lebedev, O.; Valable, S.; Mintova, S. Gadolinium-Loaded LTL Nanosized Zeolite for Efficient Oxygen Delivery and Magnetic Resonance Imaging. *Inorg. Chem. Front.* **2023**, *10* (9), 2665−2676.
(18) Hélaine, C.; Amedlous, A.; Toutain, J.; Brunaud, C.; Lebedev, O.; Marie, C.; Alliot, C.; Bernaudin, M.; Haddad, F.; Mintova, S.; Valable, S. In Vivo Biodistribution and Tumor Uptake of [64Cu]-FAU Nanozeolite via Positron Emission Tomography Imaging. *Nanoscale* **2024**, *16* (25), 11959−11968.
(19) Anfray, C.; Komaty, S.; Corroyer-Dulmont, A.; Zaarour, M.; Helaine, C.; Ozcelik, H.; Allioux, C.; Toutain, J.; Goldyn, K.; Petit, E.; Bordji, K.; Bernaudin, M.; Valtchev, V.; Touzani, O.; Mintova, S.; Valable, S. Nanosized Zeolites as a Gas Delivery Platform in a Glioblastoma Model. *Biomaterials* **2020**, *257*, No. 120249.
(20) Komaty, S.; Özçelik, H.; Zaarour, M.; Ferre, A.; Valable, S.; Mintova, S. Ruthenium Tris(2,2′-Bipyridyl) Complex Encapsulated in Nanosized Faujasite Zeolite as Intracellular Localization Tracer. *J. Colloid Interface Sci.* **2021**, *581*, 919−927.
(21) Goldyn, K.; Anfray, C.; Komaty, S.; Ruaux, V.; Hélaine, C.; Retoux, R.; Valable, S.; Valtchev, V.; Mintova, S. Copper Exchanged FAU Nanozeolite as Non-Toxic Nitric Oxide and Carbon Dioxide Gas Carrier. *Microporous Mesoporous Mater.* **2019**, *280*, 271−276.
(22) Chen, L.; Zhou, S.-F.; Su, L.; Song, J. Gas-Mediated Cancer Bioimaging and Therapy. *ACS Nano* **2019**, *13* (10), 10887−10917.
(23) Valable, S.; Gérault, A. N.; Lambert, G.; Leblond, M. M.; Anfray, C.; Toutain, J.; Bordji, K.; Petit, E.; Bernaudin, M.; Pérès, E. A. Impact of Hypoxia on Carbon Ion Therapy in Glioblastoma Cells: Modulation by LET and Hypoxia-Dependent Genes. *Cancers* **2020**, *12* (8), No. 2019.
(24) Zheng, D.-W.; Li, B.; Li, C.-X.; Fan, J.-X.; Lei, Q.; Li, C.; Xu, Z.; Zhang, X.-Z. Carbon-Dot-Decorated Carbon Nitride Nanoparticles for Enhanced Photodynamic Therapy against Hypoxic Tumor via Water Splitting. *ACS Nano* **2016**, *10* (9), 8715−8722.
(25) Komaty, S.; Daouli, A.; Badawi, M.; Ment Anfray, C.; Zaarour, M.; Valable, S.; Mintova, S. Incorporation of Trivalent Cations in NaX Zeolite Nanocrystals for the Adsorption of O_2 in the Presence of CO_2. *Phys. Chem. Chem. Phys.* **2020**, *22*, 9934.
(26) Zheng, X.-Y.; Zhao, K.; Tang, J.; Wang, X.-Y.; Li, L.-D.; Chen, N.-X.; Wang, Y.-J.; Shi, S.; Zhang, X.; Malaisamy, S.; Sun, L.-D.; Wang, X.; Chen, C.; Yan, C.-H. Gd-Dots with Strong Ligand−Water Interaction for Ultrasensitive Magnetic Resonance Renography. *ACS Nano* **2017**, *11* (4), 3642−3650.
(27) Bottrill, M.; Kwok, L.; Long, N. J. Lanthanides in Magnetic Resonance Imaging. *Chem. Soc. Rev.* **2006**, *35* (6), 557−571.
(28) Ni, D.; Shen, Z.; Zhang, J.; Zhang, C.; Wu, R.; Liu, J.; Yi, M.; Wang, J.; Yao, Z.; Bu, W.; Shi, J. Integrating Anatomic and Functional Dual-Mode Magnetic Resonance Imaging: Design and Applicability of a Bifunctional Contrast Agent. *ACS Nano* **2016**, *10* (3), 3783−3790.
(29) Yu, Y.; Xiong, G.; Li, C.; Xiao, F. S. Characterization of Aluminosilicate Zeolites by UV Raman Spectroscopy. *Microporous Mesoporous Mater.* **2001**, *46* (1), 23−34.
(30) Depla, A.; Verheyen, E.; Veyfeyken, A.; Gobechiya, E.; Hartmann, T.; Schaefer, R.; Martens, J. A.; Kirschhock, C. E. A. Zeolites X and A Crystallization Compared by Simultaneous UV/VIS-Raman and X-Ray Diffraction. *Phys. Chem. Chem. Phys.* **2011**, *13* (30), 13730−13737.
(31) Li, P.; Ding, T.; Liu, L.; Xiong, G. Investigation on Phase Transformation Mechanism of Zeolite NaY under Alkaline Hydrothermal Conditions. *Mater. Charact.* **2013**, *86*, 221−231.
(32) Ferwerda, R.; van der Maas, J. H. The Influence of Adsorbed Molecules on the Framework Vibrations of Na-Faujasites Studied with FT Raman Spectroscopy. *Spectrochim. Acta, Part A* **1995**, *51* (12), 2147−2159.
(33) Król, M.; Mozgawa, W.; Barczyk, K.; Bajda, T.; Kozanecki, M. Changes in the Vibrational Spectra of Zeolites Due to Sorption of Heavy Metal Cations. *J. Appl. Spectrosc.* **2013**, *80* (5), 644−650.
(34) Sing, K. S. W. Reporting Physisorption Data for Gas/Solid Systems with Special Reference to the Determination of Surface Area and Porosity (Recommendations 1984). *Pure Appl. Chem.* **1985**, *57* (4), 603−619.
(35) Bae, T. H.; Hudson, M. R.; Mason, J. A.; Queen, W. L.; Dutton, J. J.; Sumida, K.; Micklash, K. J.; Kaye, S. S.; Brown, C. M.; Long, J. R. Evaluation of Cation-Exchanged Zeolite Adsorbents for Post-Combustion Carbon Dioxide Capture. *Energy Environ. Sci.* **2013**, *6* (1), 128−138.
(36) Najafi, A. M.; Khorasheh, F.; Soltanali, S.; Ghassabzadeh, H. Equilibrium and Kinetic Insights into the Comprehensive Investigation of CO_2, CH_4, and N_2 Adsorption on Cation-Exchanged X and Y Faujasite Zeolites. *Langmuir* **2023**, *39* (44), 15535−15546.
(37) Walton, K. S.; Abney, M. B.; LeVan, M. D. CO_2 Adsorption in Y and X Zeolites Modified by Alkali Metal Cation Exchange. *Microporous Mesoporous Mater.* **2006**, *91* (1−3), 78−84.
(38) Xia, H.; Hu, Y.; Bao, Q.; Zhang, J.; Sun, P.; Liang, D.; Wang, B.; Qiao, X.; Wang, X. Adsorption Separation of O_2/N_2 by Li-RHO Zeolite with High Oxygen Selectivity. *Microporous Mesoporous Mater.* **2023**, *350*, No. 112442.
(39) Liu, H.; Yuan, D.; Liu, G.; Xing, J.; Liu, Z.; Xu, Y. Oxygen-Selective Adsorption on High-Silica LTA Zeolite. *Chem. Commun.* **2020**, *56* (75), 11130−11133.
(40) Wang, Y.; Helvensteijn, B.; Nizamidin, N.; Erion, A. M.; Steiner, L. A.; Mulloth, L. M.; Luna, B.; LeVan, M. D. High Pressure Excess Isotherms for Adsorption of Oxygen and Nitrogen in Zeolites. *Langmuir* **2011**, *27* (17), 10648−10656.
(41) Ene, A. B.; Bauer, M.; Archipov, T.; Roduner, E. Adsorption of Oxygen on Copper in Cu/HZSM5 Zeolites. *Phys. Chem. Chem. Phys.* **2010**, *12* (24), 6520−6531.
(42) Polisi, M.; Grand, J.; Arletti, R.; Barrier, N.; Komaty, S.; Zaarour, M.; Mintova, S.; Vezzalini, G. CO_2 Adsorption/Desorption in FAU Zeolite Nanocrystals: In Situ Synchrotron X-ray Powder Diffraction and in Situ Fourier Transform Infrared Spectroscopic Study. *J. Phys. Chem. C* **2019**, *123* (4), 2361−2369.
(43) Hattori, H.; Ono, Y.Catalysts and Catalysis for Acid−Base Reactions. *Metal Oxides in Heterogeneous Catalysis*; Elsevier B.V., 2018; pp 133−209.

https://doi.org/10.1021/acsami.4c20383
ACS Appl. Mater. Interfaces XXXX, XXX, XXX−XXX